

Raman modes of the deformed single-wall carbon nanotubes

Gang Wu,* Jian Zhou, and Jinming Dong†
Group of Computational Condensed Matter Physics,
National Laboratory of Solid State Microstructures and Department of Physics,
Nanjing University, Nanjing 210093, P. R. China
(Dated: February 1, 2008)

With the empirical bond polarizability model, the nonresonant Raman spectra of the chiral and achiral single-wall carbon nanotubes (SWCNTs) under uniaxial and torsional strains have been systematically studied by *ab initio* method. It is found that both the frequencies and the intensities of the low-frequency Raman active modes almost do not change in the deformed nanotubes, while their high-frequency part shifts obviously. Especially, the high-frequency part shifts linearly with the uniaxial tensile strain, and two kinds of different shift slopes are found for any kind of SWCNTs. More interestingly, new Raman peaks are found in the nonresonant Raman spectra under torsional strain, which are explained by a) the symmetry breaking and b) the effect of bond rotation and the anisotropy of the polarizability induced by bond stretching.

PACS numbers: 63.22.+m, 78.30.Na

I. INTRODUCTION

Single-wall carbon nanotube (SWCNT) is a kind of nanoscale molecule obtained by wrapping a graphene sheet into a seamless cylinder. Since its discovery¹ in 1991 by Iijima, the SWCNT has been of great interest in mesoscopic physics and nanotechnology because of its exceptional electronic and mechanical properties².

At the same time, much attention has been devoted to the vibrational properties of the SWCNTs^{3,4,5,6,7,8,9,10,11,12,13,14,15,16}. The excitations from the electronic density-of-state (DOS) peaks below the Fermi level to those above it are enhanced greatly due to the existence of the Van Hove singularities (VHS)¹⁷ caused by the special one-dimensional (1D) structure of the SWCNTs. As a result, the Raman spectroscopy has been considered as a powerful tool to detect the diameter-selective phonon modes of SWCNTs^{4,18,19,20}. The low-frequency peaks in the Raman spectrum are attributed to the radial breathing modes (RBM, *R* band), where all carbon atoms are subject to an in-phase radial displacement. It was found that the RBM frequency depends only on the tube diameter in an inverse proportion to it, but not on its chirality. On the other hand, the higher frequency peaks in the Raman spectrum are caused by the out-of-phase vibrations of the neighboring carbon atoms parallel to the tube surface (tangential modes, *T* band), which are related to the $E_{2g}(2)$ phonon mode at $\sim 1580 \text{ cm}^{-1}$ in graphite. In the achiral tubes, one can distinguish two tangential modes with atomic displacements parallel and perpendicular to the tube axis, respectively.

Beyond traditional force-constant method⁸, the state-of-the-art first-principle methods have already been used to calculate more accurately phonon dispersion curves^{21,22,23,24,25}, which offers a unique technique to investigate the vibrational properties of the nanotubes or nanoropes. Moreover, some of the first-principle methods can be extended to predict nonresonant Raman

intensities²⁶, which, however, needs very intensive calculations and is less accurate than the purely vibrational calculations, leading to proposal of a simple empirical bond polarizability model to calculate the Raman intensities of the fullerenes^{27,28} and nanotubes⁸. It is proved that the method can provide reasonable nonresonant Raman spectra in the most cases, including the nonresonant Raman spectra of the finite-length SWCNTs²⁹.

Recently, the mechanical deformation effect on the SWCNT electronic properties has been successfully studied by using a simple picture based on the π electron tight-binding approximation³⁰. Some interesting behaviors are found, e.g., a symmetry breaking due to the deformation may remove the degeneracy of energy levels. Experimentally, resistance of SWCNT transistors was found to vary significantly under bending and stretching³¹, and an observed torsion of a metallic SWCNT was speculated to open a small band gap of the tube³². Several theoretical studies on the uniaxially and torsionally deformed SWCNTs^{30,33,34,35,36} have shown that their band structures are determined by their chiral symmetries and the kinds of strains. Most of the deformed SWCNTs show a metal-semiconductor transition, occurring repeatedly with increasing strain. It is known that under uniaxial strain, the derivative of band gap over strain is the largest for zigzag tubes and decreases with increase of the chiral angle. In contrast, under torsional strain, the derivative becomes the largest for armchair tubes and decreases as the chiral angle decreases. In particular, armchair tubes under uniaxial strain and metallic zigzag tubes under torsional strain remain to be metallic³⁰.

At the same time, the deformation effect on the SWCNT vibration properties, especially its Raman spectroscopy, has attracted much attention in experiments^{37,38,39,40,41,42,43} and theoretical studies^{12,44}. Kahn *et al.*¹² studied the hydrostatic pressure dependence of the Raman modes for different nanotubes, and found that their shifts under pressure differ from the

corresponding ones of graphite. It is found in Refs. 37,42,43 that the RBM shifts towards higher wavenumbers with increasing hydrostatic pressure at a rate of $7\sim 10 \text{ cm}^{-1}\text{GPa}^{-1}$. With a generalized tight-binding molecular dynamics (GTBMD) scheme, Venkateswaran *et al.*⁴² analyzed the effect of the intertube Van der Waals interaction on the R band shift. And Refs. 37 and 38 reported that before a structural transition at near 2 GPa, the tangential modes exhibited essentially the same pressure dependence of 5.7-5.8 and 5.3-6.1 $\text{cm}^{-1}\text{GPa}^{-1}$, respectively. More details about this hydrostatic pressure effect on the Raman modes can be found in the review article⁴⁴. Nevertheless, all of these researches focuses on the hydrostatic pressure effect, and the uniaxial and torsional strain effects have not been studied.

In this work we will study systematically the nonresonant Raman spectra of chiral and achiral SWCNTs under uniaxial and torsional strains. The Raman intensity is calculated by using the eigenvectors of the vibrational modes obtained by *ab initio* method, and the polarizability parameters are obtained by using the empirical bond polarizability model^{8,28}. The detail of methodology is presented in Sec. II. The numerical results are discussed in Sec. III. Finally, this work ends with some conclusions in Sec. IV.

II. MODEL AND METHOD

A. Cumulant force-constant method

In most of published papers on the phonon dispersions of the SWCNTs obtained by *ab initio* calculations, the low-frequency dispersions were not well reproduced mainly due to use of the interatomic force-constant (IFC) method. In Ref. 25, by means of Cumulant Force Constant (CFC) method, L. H. Ye *et al.* successfully calculated phonon dispersions of the nanotubes and graphite. Details about comparison between the CFC and IFC

methods are available in their original paper²⁵. In this work, we use CFC method to construct the dynamical matrices for both of the undeformed and deformed SWCNTs, and then calculate their phonon dispersion curves.

First, we summarize the reason of employing CFC method in this work:

a). The 1D-like geometrical structure of the carbon nanotube makes its physical properties highly anisotropic, for which it is definitely necessary to use the CFC instead of the IFC. Comparatively, the CFC is also an approximated method, but it keeps the most rotational symmetries, which means although the numerical values of the dynamical matrices are obtained approximately, the symmetries of the dynamical matrices are correct. This is the reason why it works so well for an anisotropic system.

b). In the IFC method, in order to minimize the truncation effect, one should use a large supercell, spending much computational time. At the same time, the numerical noise in force calculations may become very serious if too large supercell is used, which may reduce the accuracy of phonon calculation. On the other hand, because the CFC method does not need to perform an explicit truncation on the interatomic interactions, as shown in Ref. 25, so, only a very small supercell (1x1x2) in the CFC method is sufficient to calculate accurately the phonon modes on the Γ point and the X point at Brillouin zone boundary. This also means that the phonon modes of even achiral SWCNTs, such as (12, 4) tube containing 208 atoms in its one unit cell, can be efficiently calculated under current hardware conditions.

B. Empirical bond polarizability model

The time-averaged power flux of the Raman-scattered light at a given direction of a solid angle $d\Omega$ in a frequency range between ω_f and $\omega_f + d\omega_f$ is related to the differential scattering cross section as follows,

$$\frac{d^2\sigma}{d\Omega d\omega_f} = \frac{1}{8\pi^2 c^2} \omega_f^3 \omega_i [\langle n(\omega) \rangle + 1] \hbar \times \sum_{\alpha\beta\gamma\lambda} v_\alpha v_\beta H_{\alpha\gamma\beta\lambda}(\omega) w_\gamma w_\lambda, \quad (1)$$

where

$$H_{\alpha\gamma\beta\lambda}(\omega) = \sum_j a_{\alpha\gamma}^*(j) a_{\beta\lambda}(j) \frac{1}{2\omega_j} [\delta(\omega - \omega_j) + \delta(\omega + \omega_j)], \quad (2)$$

with

$$a_{\alpha\gamma}(j) = \sum_{n\delta} \frac{\pi_{\alpha\gamma,\delta}^n}{\sqrt{M_n}} \langle \delta n | j \rangle. \quad (3)$$

Here, ω_i and ω_f are the frequencies of the incident and scattered light; $\omega \equiv \omega_i - \omega_f$ is the Raman shift. \vec{v} and \vec{w} are the corresponding polarization unit vectors of the incident and scattered light, respectively. $\langle n(\omega) \rangle$ is the Bose factor, M_n is the mass of the n th atom, and

ω_j and $\langle \delta n | j \rangle$ are the frequency and (δn) component of the j th mode. The coefficient $\pi_{\alpha\gamma,\delta}^n$ in Eq. (3) connects the polarization changes to the atomic motions⁴⁷, which is obtained by expanding the polarizability tensor π^n in terms of the atom displacements u_δ^n , with

$$\pi_{\alpha\gamma,\delta}^n = \sum_m \left(\frac{\partial \pi_{\alpha\gamma}^m}{\partial u_\delta^n} \right)_0. \quad (4)$$

$$\pi_{\alpha\beta,\gamma}^n = \sum_m \frac{(2\alpha'_{\parallel} + \alpha'_{\perp})}{3} \delta_{\alpha\beta} \hat{r}_\gamma + (\alpha'_{\parallel} - \alpha'_{\perp}) \left(\hat{r}_\alpha \hat{r}_\beta - \frac{1}{3} \delta_{\alpha\beta} \right) \hat{r}_\gamma + \frac{(\alpha_{\parallel} - \alpha_{\perp})}{r} (\delta_{\alpha\gamma} \hat{r}_\beta + \delta_{\beta\gamma} \hat{r}_\alpha - 2\hat{r}_\alpha \hat{r}_\beta \hat{r}_\gamma). \quad (5)$$

Here, \hat{r} is the unit vector of the vector \vec{r} connecting the n and m atoms linked by a bond. α_{\parallel} and α_{\perp} represent the static longitudinal and perpendicular bond polarizability, respectively, and $\alpha'_{\parallel} = \left(\frac{\partial \alpha_{\parallel}}{\partial r} \right)_0$, $\alpha'_{\perp} = \left(\frac{\partial \alpha_{\perp}}{\partial r} \right)_0$. The values of α_{\parallel} , α_{\perp} , α'_{\parallel} and α'_{\perp} are given empirically as a function of the bond length between two carbon atoms. For undeformed SWCNTs, there is only single type of bonds and the bond polarizability model is completely defined by three parameters⁸: $\alpha = 2\alpha'_{\parallel} + \alpha'_{\perp} = 4.7 \text{ \AA}^2$, $\beta = \alpha'_{\parallel} - \alpha'_{\perp} = 4.0 \text{ \AA}^2$, and $\gamma = \alpha_{\parallel} - \alpha_{\perp} = 0.04 \text{ \AA}^3$. It is known, however, that the polarizability parameters of carbon are similar for a variety of carbon materials. Furthermore, the relative intensities of the Raman modes are not so sensitive to small changes of the bond polarization parameter values, except for the lowest E_{2g} mode. Thus in the present work, we still use the above polarization parameters for the deformed SWCNTs, which can only lead to a small error in the peak height, and does not affect the peak positions. In fact, Guha et al.²⁸ chose different bond polarizability parameters to calculate the Raman spectra of the fullerenes, causing only small changes of the relative Raman intensities, which is also found in our calculations. For example, even use of a set of parameters obtained by interpolating those of the fullerenes and nanotubes does not bring any qualitative changes of our results.

In all our calculations, the line shape of each peak is assumed to be Lorentzian and its line-width is fixed at 1.68 cm^{-1} . The tube axis is taken along the Z direction, and the X and Y directions are taken to be perpendicular to it. In Ref. 8, two possible geometries for the light polarization are mentioned: the VV and VH configurations. In the VV configuration, the incident and the scattered polarizations are parallel to each other, while they are perpendicular to each other in the VH configuration. After careful calculations, we can find all of the Raman-active peaks in the VV configuration. For the VH configuration, there is no any qualitative change of our results compared with those obtained from VV con-

figuration. Adopting the nonresonant empirical bond-polarization theory^{8,27,28}, the Eq. (4) can be rewritten as:

figuration. Due to this reason, and also because we pay our main attention to the shift of the Raman mode frequency under applied strains, only the results in the VV configuration have been presented in this work.

C. Calculation details

Our first principle calculations are based on the total energy plane-wave pseudopotential method in the local density approximation (LDA). The Vienna *ab initio* simulation package (VASP)^{48,49} is employed in this paper. In the most recent version of VASP, the interaction between the ions and electrons is described by the projector augmented-wave⁵⁰ (PAW) in the implementation of Kress and Joubert⁵¹. The PAW method is always considered to be able to give a more accurate and reliable result than the ultrasoft potential. In the present PAW potential, the $2s$ and $2p$ orbitals are treated as valence orbitals, and a plane-wave cutoff of 400 eV is used to obtain reliable results.

A supercell geometry was adopted so that the nanotubes are aligned in a hexagonal array with the closest distance between adjacent nanotube surfaces being at least 10 Å, which is found to be large enough to prevent the tube-tube interactions.

The K-points sampling in the reciprocal space is a uniform grid ($1 \times 1 \times n$) along the nanotube axis (Z direction) in our calculations, the maximum spacing between k points is 0.03 \AA^{-1} and the Gaussian smearing width is 0.03 eV. This means that n is obtained by dividing 30 with the supercell length along the tube axis. For example, for a supercell ($1 \times 1 \times 2$) constructed by the unit cell of a zigzag tube, the n equals to $30/(T_{zig} * 2) \approx 6$, where $T_{zig} \approx 2.451 \text{ \AA}$ is the unit cell length of the zigzag tube. The increasing K-points sampling has no significant effect on the frequencies of the final Raman active modes, e.g., doubling the number of special k points only causes less than 4 cm^{-1} change on the most Γ point phonon frequencies.

All SWCNT geometrical structures used in this work have been fully optimized before performing further force constants (FCs) calculation. The structural optimization process is almost the same as Ref. 25. Finally, the optimal structure is obtained when the residue forces acting on all the atoms were less than 0.005 eV/Å for achiral SWCNTs and 0.01 eV/Å for chiral SWCNTs. The equilibrium lattice constants and averaged nanotube radii are listed in Table I. Our structure parameters of (5, 5), (10, 0) and (10, 5) tubes are almost the same as those in Ref. 53, which are also obtained by VASP.

Due to the high symmetry of an ideal SWCNT, so there exists only one inequivalent atom. Thus the FCs of one atom are sufficient to construct the force constant matrix of the whole tube by applying the tube symmetry.

TABLE I: Optimized structural parameters of the undeformed nanotubes. R_0 is the average radius, and T_0 is the lattice constant along the tube axis.

Tubes	$R_0(\text{\AA})$	$T_0(\text{\AA})$
(6, 0)	2.397	4.230
(7, 0)	2.773	4.235
(8, 0)	3.159	4.233
(9, 0)	3.541	4.237
(10, 0)	3.927	4.237
(11, 0)	4.313	4.238
(5, 5)	3.408	2.448
(6, 6)	4.075	2.448
(10, 5)	5.173	11.21
(12, 4)	5.636	15.28

III. NUMERICAL RESULTS AND DISCUSSIONS.

In this section, the Raman spectra of the infinite-length deformed SWCNTs are investigated. Firstly, the tensile strain effect will be discussed in Sec. III A, and the torsional strain one will be given in Sec. III B.

A. Tensile strain

The phonon dispersion relations and density of states for zigzag (10, 0) tube are shown in Fig. 1, from which, one can find that the low-frequency dispersions are well produced, and when the tensile strain is applied, the low-frequency vibration modes almost do not change, while the high-frequency vibrations show sensitive response to the tensile strain.

These characters can be seen more clearly in the Raman spectra. First we will consider the Raman spectra of zigzag tubes as an example. Because the cylindric structure and the neighboring relationships do not change under the tensile strain, we find the intensities of the Raman active modes almost do not change at all. Thus only

the frequency shifts for the Raman active modes under tensile strain are given in Fig. 2. In the present work, the tensile strain is defined as $e = (T/T_0) - 1$, where T and T_0 are the lengths of the axial unit cells of the deformed and undeformed nanotubes, respectively. The values of T_0 have been given in Table I. After applying tensile strain, only the positions of the carbon atoms are relaxed to obtain a reliable optimized structure. It can be seen clearly from Fig. 2 that when the tensile strength increases: a) The frequencies of the low-frequency Raman active modes almost do not change. While the high-frequency part of the Raman spectra is shifted downward, which consists with the available experimental and theoretical results^{12,37,38,39,40,41,42,43,44}. b) The deformation does not change the number of the Raman active vibrations. c) The shifting rate of the Raman modes is almost the same for the nanotubes with different radii, i.e., they shift linearly.

In fact, above three results are reasonable and can be understood as follows. Because different nanotubes have almost the same Poisson ratio σ of 0.2, the tube radius only changes about 1%, even if the tube is elongated by 5%. And for lower Raman modes, the vibrational frequencies are mainly affected by the tube diameter, making their peak positions do not move much. Especially, for the radial breathing mode (RBM), which is found to be inversely proportional to the tube diameter, only very small shift (about 1 cm⁻¹) is found when the tensile strength increases up to 5%.

But the bonds parallel to the tube axis will be elongated when tensile strain is applied. For higher Raman frequencies, the vibrations are sensitive to the local bond structure, especially its length. When bond length is elongated, the interaction among nearby atoms will become weaker, making the Raman frequency smaller.

Now we would like to discuss why the number of Raman active modes does not change under the tensile strain. Following the discussion of Ref. 52, the number of Raman active modes can be determined by using the nonsymmorphic rod-groups of SWCNTs. All achiral carbon nanotubes can be shown by this method to possess only 8 Raman-active phonon modes⁵², and for all chiral carbon nanotubes, 14 Raman-active modes can be found. Furthermore, for the first-order Raman scattering, the point group is sufficient because this process does not change the wave vector k . Another fact is that the point groups of achiral (zigzag or armchair) and chiral SWCNTs are D_{2nh} and D_N , respectively, where n is the tube index and N is the number of graphene hexagons in the nanotube unit cell. These point groups do not change under tensile strain. Correspondingly, simply following the discussion in Ref. 52, one can conclude that when tensile strength increases, the Raman active vibration number of zigzag nanotubes will keep 8, which has been shown by our numerical results.

Then let us analyze the detail of frequency shift of Raman active modes. From Fig. 2, one can find that the modes below 1000 cm⁻¹ is insensitive to the tensile

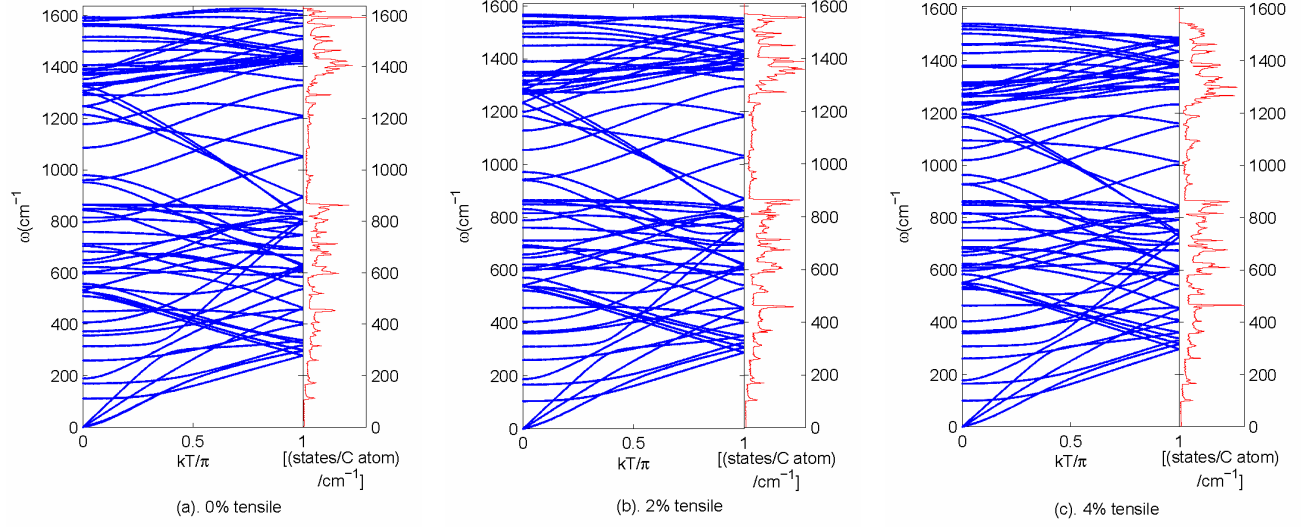


FIG. 1: Calculated phonon dispersion curves and density of states are shown in the left and right panels, respectively, in each sub-figure. For (10, 0) zigzag nanotube under the tensile strains of 0%, 2% and 4%.

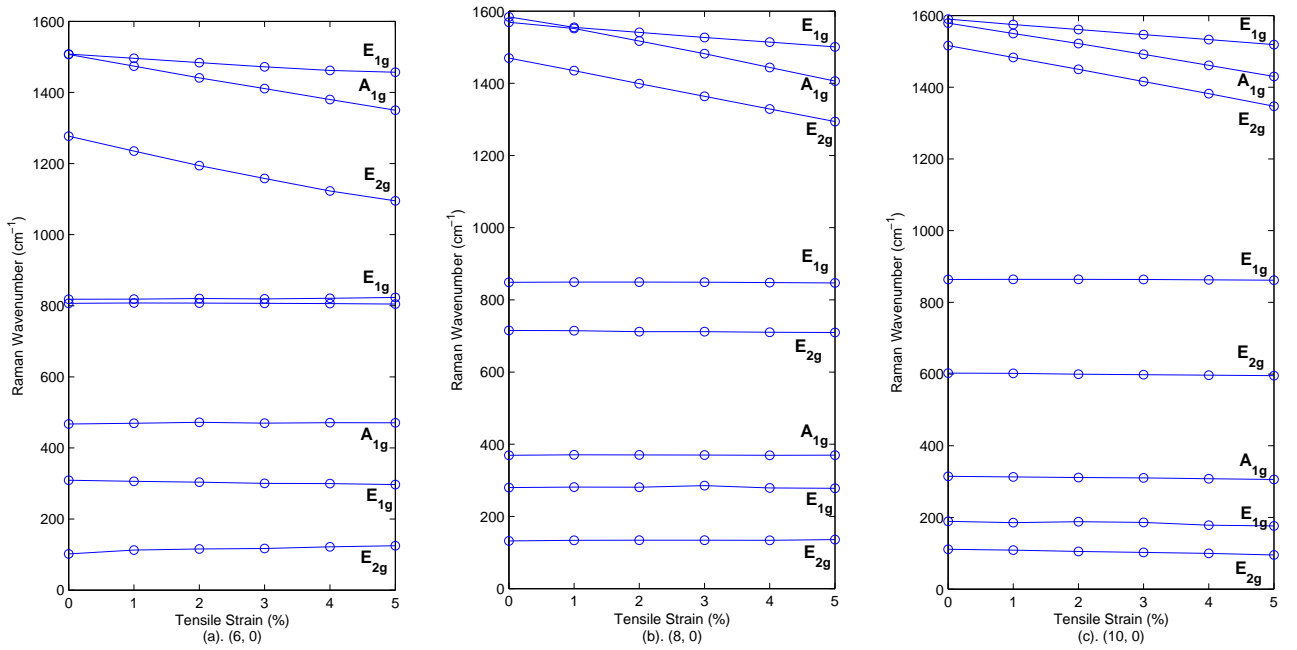


FIG. 2: Frequencies of Raman active modes for (n, 0) zigzag tubes (n=6, 8 and 10) under tensile strain.

strain. And above 1000 cm^{-1} , the frequencies of Raman active modes decrease linearly with tensile strain, for which there exist two different decreasing slopes for: (i). E_{1g} , and (ii). E_{2g} and A_{1g} modes.

Similar phenomenon has been found in the graphite system⁵⁴. Following Ref. 54, we also calculated the Grüneisen tensor elements (GTEs) $\kappa = -\frac{d \ln \omega}{d \ln(1+e)}$, where ω is the frequency of Raman active modes, and e is the

tensile strain. We plot the GTEs vs the tube index n of the zigzag tubes in Fig. 3, and further fit them with a same fitting function in the same plot. The fitting function is obtained based on the following factors: a) The GTEs must have the same dependence on the tube radii as the frequencies of Raman modes. In Ref. 55, the higher Raman frequencies depend on the tube radius via the confined wave vector q around the equa-

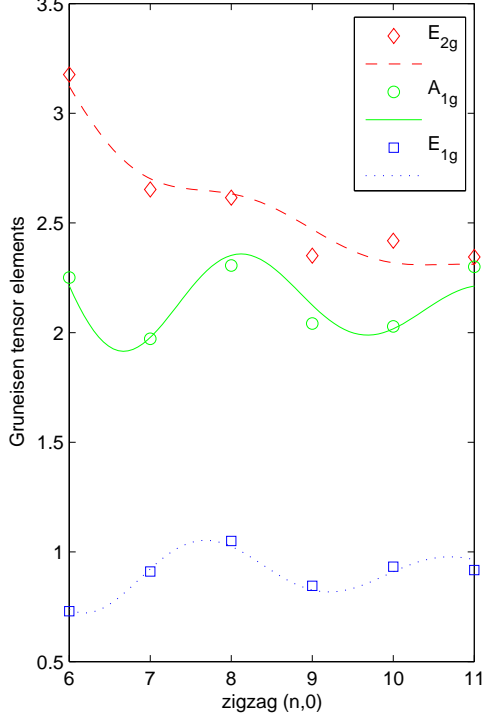


FIG. 3: (Color online) The GTEs for the highest three Raman active modes of zigzag tubes $(n, 0)$, $(n = 6, \dots, 11)$. The lines are fitting results (see text), and other markers (circles, diamonds and squares) are GTEs obtained by first-principle calculations.

torial direction, where $q \propto 1/r \propto 1/n$. Here we following this idea and set the nonoscillating part of the fitting function as $A + \frac{B}{n^2}$, where A and B are undetermined coefficients, whose quadratic form fulfils the phonon dispersion near the Γ point of graphite. b) The above κ form still can not describe the oscillating behavior of the GTEs. Thus an extra oscillating term must be added into the fitting function, which can be written as $\frac{C}{n^2} \sin(\frac{2\pi}{3}n + \phi_0)$, where the period has been set as 3 to match the oscillating period of the energy gap of zigzag tubes, and the denominator n^2 is used to let this term quickly vanish when $n \rightarrow \infty$. So the final fitting function can be written as: $\kappa = A + \frac{B}{n^2} + \frac{C}{n^2} \sin(\frac{2\pi}{3}n + \phi_0)$. After making a simple least-squares fit, finally we can obtain $\kappa_{E_{1g}}(r \rightarrow \infty) = 0.897$, $\kappa_{A_{1g}}(r \rightarrow \infty) = 2.05$, and $\kappa_{E_{2g}}(r \rightarrow \infty) = 1.95$, which can be checked by future experiments. This also offers a powerful tool to determine the strength of the tensile strain, i.e., after detecting the Raman-active modes under undeformed and deformed conditions, one can easily estimate how big the applied tensile strain is.

Next, let us consider the armchair and chiral SWCNTs. We find those three key characters found for the Raman spectra of zigzag tubes are also hold for these

SWCNTs. The reason should be the same as that for the zigzag tubes. Because we mainly concern the frequency shift, so the Raman spectra will not be shown, and instead only the frequencies of the Raman active modes for some armchair and chiral tubes under tensile strains are shown in Fig. 4, which can already represent all the key characters clearly.

The GTEs for these tubes are also calculated. It is interesting to note that the GTEs of the high-frequency Raman modes of armchair tubes can also be divided into two groups, and their values are very close to those of the zigzag tubes. For example, for $(6, 6)$ tube, $\kappa_{E_{1g}} = 2.35$, $\kappa_{A_{1g}} = 0.861$, and $\kappa_{E_{2g}} = 0.794$. And for $(12, 4)$ tube, the GTEs of the six highest frequency Raman modes are: 2.25, 2.27, 2.28, 0.994, 0.907 and 0.846. So, we suppose that for any SWCNTs, there are only two kinds of GTEs for the high-frequency Raman modes. In fact, detailed analysis shows that those modes with the larger GTEs are the tangential with atomic displacements parallel to the tube axis, and those modes with the smaller GTEs are the tangential modes with atomic displacements perpendicular to the tube axis. This fact could be clearly seen from Fig. 5, showing the atomic displacements of three high-frequency Raman-active tangential modes of $(6, 6)$ tube.

Finally, one may notice that it is different for the tensile strain to affect the electronic and vibrational properties of SWCNTs. As mentioned in the introduction part, most of the deformed SWCNTs show a metal-semiconductor transition, occurring repeatedly with increasing strain. Correspondingly, the linear optical responses of the deformed carbon nanotubes also show periodical change with increasing strain⁵⁶. But as shown in our calculations, the frequencies of Raman active modes change monotonously with applied tensile strain and their intensities only change very little, which is consistent with the available experiments^{37,38,39,40,41,42,43,57}.

B. Torsional strain

In this part, the torsional strain effect on the Raman modes is investigated. Here, three tubes with different chiralities are taken as an example, i.e., armchair $(5, 5)$, zigzag $(10, 0)$ and chiral $(12, 4)$ tubes. The torsion angle γ is defined in a similar way to that in Ref. 30, i.e., it makes any point (r_c, r_t) on the 2D projection of the tube surface move to $(r_c - \tan(\gamma)r_t, r_t)$ (see Fig. 6). The following method is used to find a new periodical structure under torsional strain: firstly, an origin of the coordinates is selected as the site O , from which, we can define a chiral vector \vec{C} and the original translational vector \vec{T}_0 . Then, we find an equivalent site B for the site O . By projecting the vector \vec{OB} to the \vec{T}_0 , a new translational vector $\vec{OB'}$ can be produced as a tube period, and the angle between \vec{OB} and $\vec{OB'}$ is the corresponding torsion angle γ . After structure relaxation on both the lattice

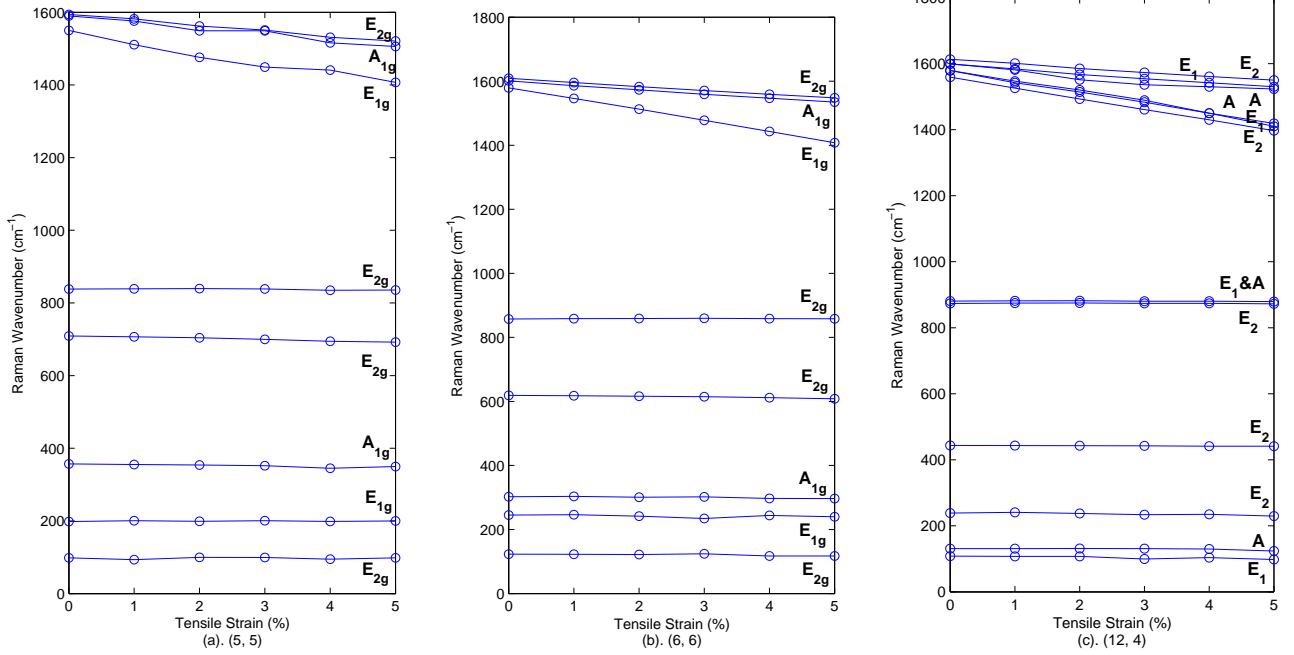


FIG. 4: Frequencies of Raman active modes for some armchair and chiral SWCNTs under tensile strain. (a) (5, 5), (b) (6, 6), (c) (12, 4).

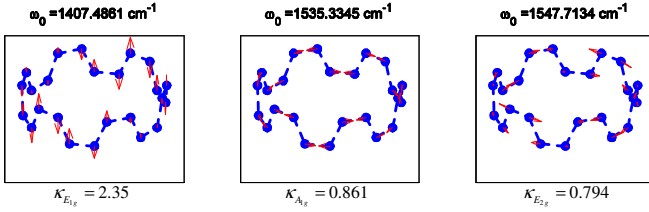


FIG. 5: (Color online) The atomic displacements of three Raman-active tangential modes of (6, 6) tube. ω_0 is the frequency of Raman-active modes of undeformed tube.

constant along the tube axis and the atomic positions, we can finally obtain a reasonable structure which can be used for further first principle calculations. And in all of our calculations, the system keeps a cylinder structure and does not appear any structure transformations⁵⁸ or defects⁵⁹.

The Raman spectra of different SWCNTs under torsional strain have been shown in Fig. 7. Because of the symmetry, we only consider the case of positive γ for the armchair and zigzag tubes. Compared with the situation under the tensile strain, we can find two similar key characters: a) Not only the frequencies of the low-frequency Raman active modes, but also their intensities almost do not change. Some of the high-frequency modes in the Raman spectra are red-shifted and some ones are blue-shifted. b) The Raman active vibration number changes under torsional strain.

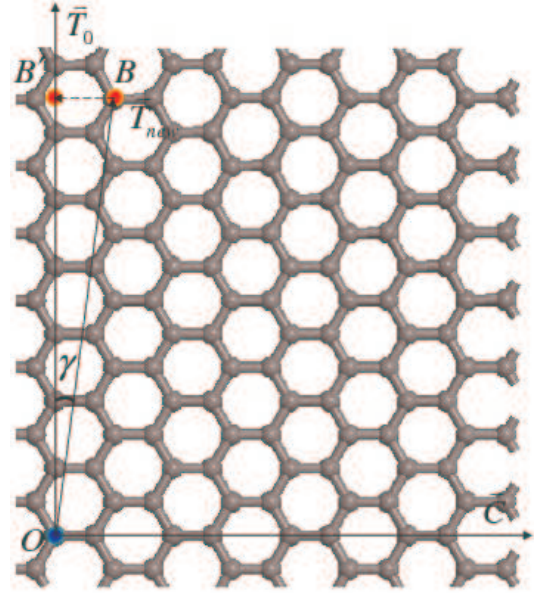


FIG. 6: (Color online) 2D projection of the nanotubes under the torsional strain, where γ is the torsion angle and \vec{C} is the chiral vector. \vec{T}_0 and \vec{T}_{new} are the translational vectors for the undeformed and the deformed tube.

In fact, the first character can be explained by the same reason as that under tensile strain. For example, the radii of the optimized (12, 4) tubes changes only about 0.2%

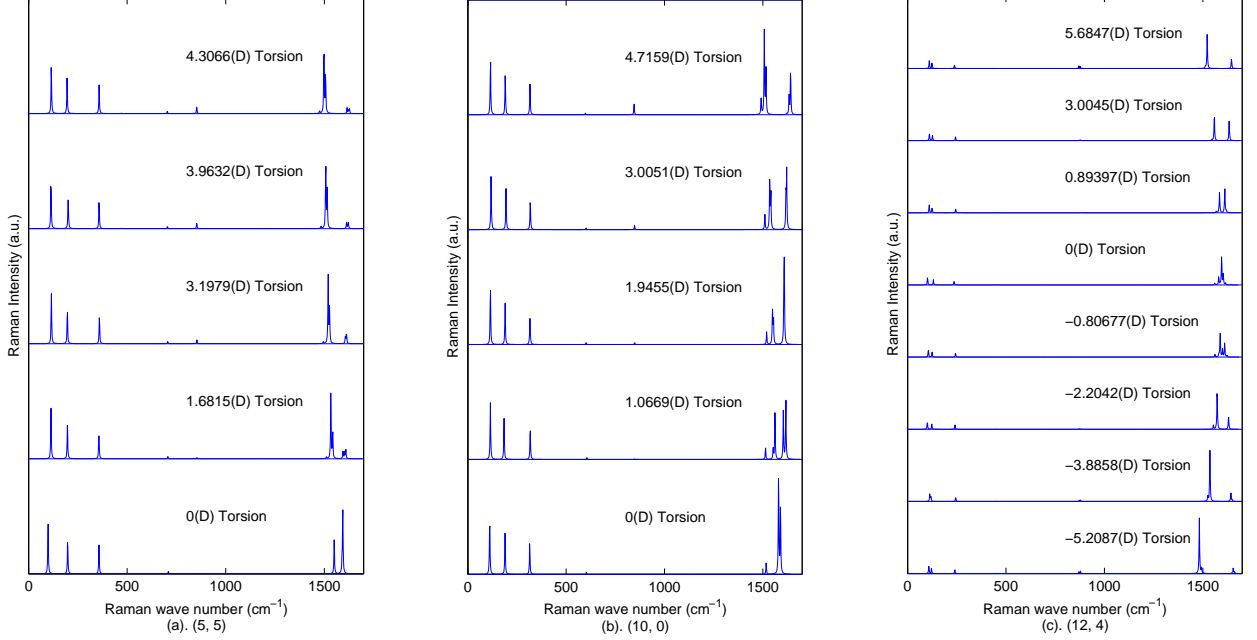


FIG. 7: The Raman spectra of different SWCNTs under torsional strain. (a) (5, 5), (b) (10, 0), (c) (12, 4).

when the torsional strain is increased up to 6° . And the two bonds mirroring each other with σ_v symmetry (see Fig. 1 of Ref. 52) will be elongated and shortened under the torsional strain, respectively, making thus some Raman modes red-shifted, and some others blue-shifted. The second character may be not so obvious like the first one. In fact, this character manifests itself in two different ways, originating from different mechanisms. The frequencies of Raman active modes for the three tubes under torsional strains are shown in Fig. 8, from which, it is seen that in the range from 1400 to 1600 cm^{-1} for all the tubes, some modes split into two new modes, obviously arising from symmetry breaking. Since the torsional strains applied in this work is smaller, the two new modes are very close to each other.

On the other hand, some new low-frequency modes (about 400 cm^{-1}) appear in the zigzag tubes, which can not simply explained by symmetry breaking. In order to find the origin of these new modes, the separate contributions to the Raman intensities from the three different terms in Eq. (5) are investigated. The same technique had been used in Ref. 28 to gain a deeper insight into the significance of the separate contributions due to different hydrocarbon parameters and the fit parameters for C_{60} . Only the results under torsional strain are given in Fig. 9 because the three parts vanish in undeformed SWCNTs. From Fig. 9, one can find that the torsional strain do break the forbidden rule of these modes⁵² and affect their Raman intensity dramatically. With torsional strain, the contributions from the second and the third term in Eq. (5) enhance greatly. The second term in Eq. (5) corre-

sponds to the contribution from the anisotropic part of the polarizability under bond stretching, and the third term corresponds to the contribution from bond rotation. Obviously, the three bonds are elongated differently under torsional strain, which means the anisotropic effect will be important. And because torsional strain makes the bonds rotate, the third term will also enhance. Altogether, the scattering cross section and thus the total Raman intensity at a specific frequency will increase under torsional strain.

Finally, the GTEs of high-frequency Raman modes of these tubes under torsional strain are calculated, which are defined in the present work as $\kappa_t = -\frac{16}{3} \frac{d \ln \omega}{d \tan^2 \gamma}$. Here, ω is the frequency of Raman-active modes, and γ is the torsional strain. This definition is obtained by assuming $\frac{\omega}{\omega_0} = \left[\frac{r}{r_0} \right]^{3\kappa_t}$, which is taken from Ref. 54. The κ_t for the 4 highest Raman-active modes of (5, 5) tube are found to be -26.73, -26.52, 19.85 and 15.65, respectively, and κ_t for the 5 highest Raman-active modes of (10, 0) tube are -13.68, -30.68, -28.37, 17.95 and 19.80, respectively. Because of the complexity of the high-frequency Raman modes of (12, 4) tube, here only its two most intense modes at about 1600 cm^{-1} are considered, whose κ_t are -32.29 and 14.03. One can find that these values do not obviously relate to each other, which is different from those under the tensile strain. So, more investigations should be done to find the intrinsic mechanism to cause the shifts of the Raman-active modes under torsional strain.

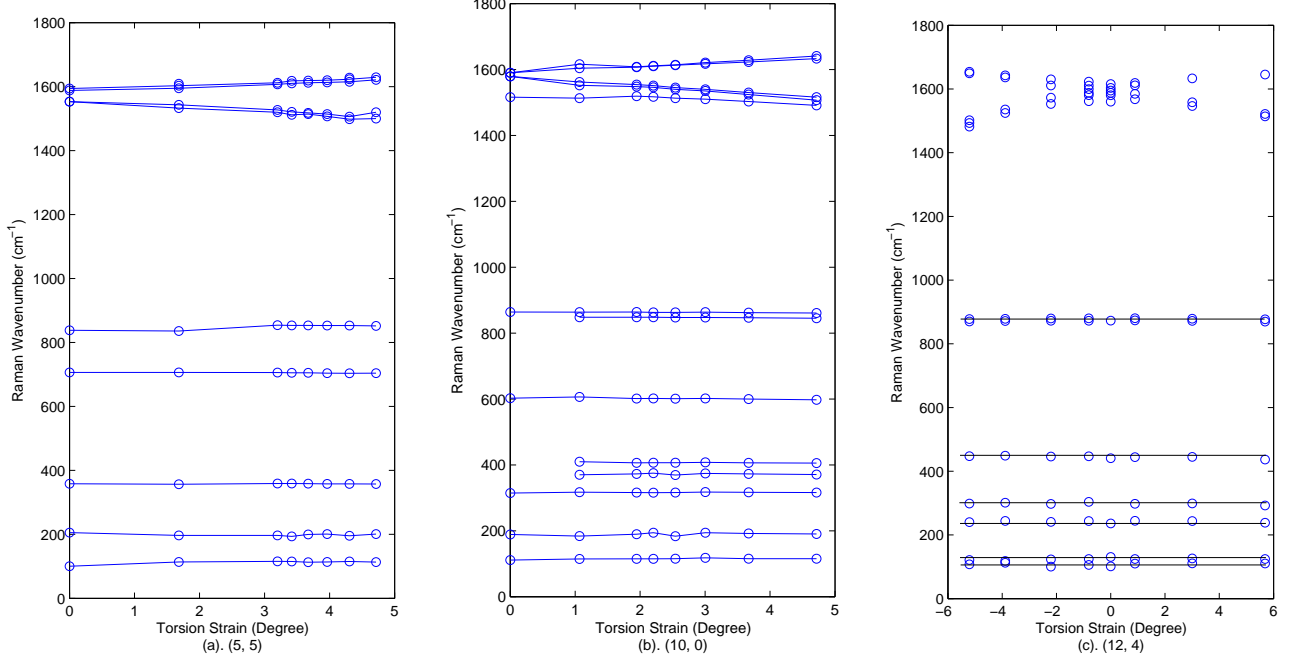


FIG. 8: Frequencies of Raman active modes vs torsional strains for three SWCNTs. (a) (5, 5), (b) (10, 0), (c) (12, 4).

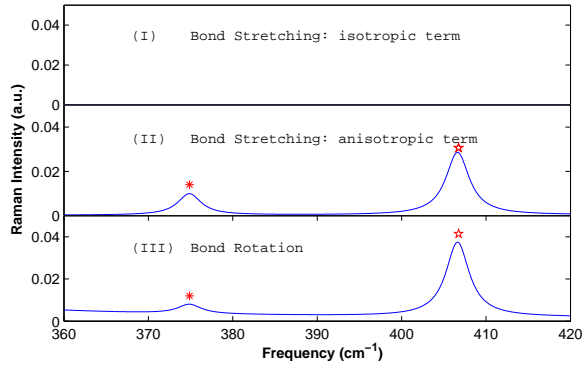


FIG. 9: (Color online) Raman peak intensities of deformed (10, 0) tube with torsional angle of 2.2047° , contributed from the three individual terms in Eq. (5). The asterisk and pentagram indicate the positions of new Raman-active modes. Panel (I), (II) and (III) give the contributions from the first, the second and the last term in Eq. (5), respectively. Notice that the total intensity is not the sum of those in the three panels due to interference effects between them.

IV. CONCLUSIONS

In this paper, the nonresonant Raman spectra of chiral and achiral SWCNTs under uniaxial and torsional strains have been systematically studied by the *ab initio* calculations and the empirical bond polarizability model. The

cumulant force-constant method is used to construct the dynamical matrices. Under tensile strain, it is found that the frequencies and the intensities of the low-frequency Raman active modes almost do not change, while their high-frequency part shifts downward linearly with two different slopes for any kind of SWCNTs. And the Raman active vibration number does not change under the tensile strain. Under the torsional strain, the frequencies and the intensities of the low-frequency Raman active modes still change very little, but some of the high-frequency modes are red-shifted and some others blue-shifted. More importantly, new Raman peaks are found in the nonresonant Raman spectra under torsional strain, which are explained by a) the symmetry breaking and b) the effect of bond rotation and the anisotropy of the polarizability induced by bond stretching.

Acknowledgments

The authors acknowledge support from the Natural Science Foundation of China under Grants No. 10474035 and No. A040108. The authors also thanks support to this work from a Grant for State Key Program of China through No. 2004CB619004. Gang Wu would like to thank Dr. Ye Linhui for useful discussions on CFC method. Our calculations have been done on the Sun Fire V20z computers.

- * Electronic address: wugaxp@gmail.com
† Corresponding author E-mail: jdong@nju.edu.cn
- ¹ S. Iijima, *Nature (London)* **354**, 56(1994).
 - ² M.S. Dresselhaus, G. Dresselhaus, and Ph. Avouris, *Carbon Nanotubes: Synthesis, Structure, Properties and Applications*, Vol. 80 of Springer Series in Topics in Applied Physics (Springer-Verlag, Berlin, 2001).
 - ³ M. S. Dresselhaus and P. C. Eklund, *Adv. Phys.* **49**, 705 (2000).
 - ⁴ A. M. Rao, E. Richter, S. Bandow, B. Chase, P. C. Eklund, K. A. Williams, S. Fang, K. R. Subbaswamy, M. Menon, A. Thess, R. E. Smalley, G. Dresselhaus, and M. S. Dresselhaus, *Science* **275**, 187 (1997).
 - ⁵ A. Kasuya, Y. Sasaki, Y. Saito, K. Tohji, and Y. Nishina, *Phys. Rev. Lett.* **78**, 4434 (1997).
 - ⁶ J. Hone, B. Batlogg, Z. Benes, A. T. Johnson, and J. E. Fischer, *Science* **289**, 1730 (2000).
 - ⁷ R. A. Jishi, L. Venkataraman, M. S. Dresselhaus, and G. Dresselhaus, *Chem. Phys. Lett.* **209**, 77 (1993).
 - ⁸ R. Saito, T. Takeya, T. Kimura, G. Dresselhaus, and M. S. Dresselhaus, *Phys. Rev. B* **57**, 4145 (1998).
 - ⁹ R. Saito, T. Takeya, T. Kimura, G. Dresselhaus, and M. S. Dresselhaus, *Phys. Rev. B* **59**, 2388 (1999).
 - ¹⁰ V. P. Sokhan, D. Nicholson, and N. Quirke, *J. Chem. Phys.* **113**, 2007 (2000).
 - ¹¹ V. N. Popov, V. E. Van Doren, and M. Balkanski, *Phys. Rev. B* **59**, 8355 (1999); **61**, 3078 (2000).
 - ¹² D. Kahn, and J. P. Lu, *Phys. Rev. B* **60**, 6535 (1999).
 - ¹³ D. Kahn, K. W. Kim, and M. A. Strosico, *J. Appl. Phys.* **89**, 5107(2001).
 - ¹⁴ M. Xia, S. Zhang, S. Zhao, and E. Zhang, *Physica B* **344**, 66(2004).
 - ¹⁵ G. D. Mahan, *Phys. Rev. B* **65**, 235402 (2002).
 - ¹⁶ S. Zhang, M. Xia, S. Zhao, T. Xu, and E. Zhang, *Phys. Rev. B* **68**, 075415 (2003).
 - ¹⁷ J.W. Mintmire, B. I. Dunlap, and C. T. White, *Phys. Rev. Lett.* **68**, 631 (1992); N. Hamada, S.I. Sawada, and A. Oshiyama, *Phys. Rev. Lett.* **68**, 1579 (1992); R. Saito, M. Fujita, G. Dresselhaus, and M. S. Dresselhaus, *Phys. Rev. B* **46**, 1804 (1992).
 - ¹⁸ C. Journet, W.K. Maser, P. Brenier, A. Loiseau, M. Lamy de la Chapelle, S. Lefrant, P. Deniard, R. Lee, and J.E. Fischer, *Nature (London)* **388**, 756 (1997).
 - ¹⁹ J.M. Holden, Ping Zhou, Xiang-Xin Bi, P.C. Eklund, Shunji Bandow, R.A. Jishi, K. Das Chowdhury, G. Dresselhaus, and M.S. Dresselhaus, *Chem. Phys. Lett.* **220**, 186 (1994).
 - ²⁰ A.G. SouzaFilho, S.G. Chou, G.G. Samsonidze, G. Dresselhaus, M.S. Dresselhaus, L. An, J. Liu, A.K. Swan, M.S. Unlu, B.B. Goldberg, A. Jorio, A. Gruneis, and R. Saito, *Phys. Rev. B* **69**, 115428 (2004).
 - ²¹ P. Pavone, K. Karch, O. Schütt, W. Windl, D. Strauch, P. Giannozzi, and S. Baroni, *Phys. Rev. B* **48**, 3156 (1993).
 - ²² G. Kresse, J. Furthmüller, and J. Hafner, *Europhys. Lett.* **32**, 729 (1995).
 - ²³ D. Sánchez-Portal, E. Artacho, J.M. Soler, A. Rubio, and P. Ordejón, *Phys. Rev. B* **59**, 12 678 (1999).
 - ²⁴ O. Dubay and G. Kresse, *Phys. Rev. B* **67**, 035401 (2003).
 - ²⁵ L.H. Ye, B.G. Liu, D.S. Wang, and R. Han, *Phys. Rev. B* **69**, 235409 (2004).
 - ²⁶ Paolo Giannozzi and Stefano Baroni, *J. Chem. Phys.* **100**, 8537 (1994).
 - ²⁷ S. Sanguinetti, G. Benedek, M. Righetti, and G. Onida, *Phys. Rev. B* **50**, 6743 (1994).
 - ²⁸ S. Guha, J. Menendez, J.B. Page, and G.B. Adams, *Phys. Rev. B* **53**, 13106 (1996).
 - ²⁹ A. Rahmani, J.-L. Sauvajol, S. Rols, and C. Benoit, *Phys. Rev. B* **66**, 125404 (2002).
 - ³⁰ Liu Yang and Jie Han, *Phys. Rev. Lett.* **85**, 154 (2000); Liu Yang, M.P. Anantram, Jie Han, and J.P. Lu, *Phys. Rev. B* **60**, 13874 (1999).
 - ³¹ W. Thomas et al, *Appl. Phys. Lett.* **76**, 2414 (2000).
 - ³² W. Clauss, D.J. Bergeron, and A.T. Johnson, *Phys. Rev. B* **58**, R4266 (1998).
 - ³³ R. Heyd, A. Charlier, E. McRae, *Phys. Rev. B* **55**, 6820 (1997).
 - ³⁴ D.W. Brenner, J.D. Schall, J.P. Mewkill, D.A. Shenderova, S.B. Sinnott, *Interplanet. Soc.* **51**, 137 (1998).
 - ³⁵ C.L. Kane, E.J. Mele, *Phys. Rev. Lett.* **78**, 1932 (1997).
 - ³⁶ W. Fa, J. Dong, *Phys. Rev. B* **70**, 233407 (2004).
 - ³⁷ M. J. Peters, L.E. McNeil, Jian Ping Lu, and Daniel Kahn, *Phys. Rev. B* **61**, 5939 (2000).
 - ³⁸ S. Reich, H. Jantoljak, and C. Thomsen, *Phys. Rev. B* **61**, R13389 (2000).
 - ³⁹ J. Sandler, M.S.P. Shaffer, A. H. Windle, M.A. Montes-Moran, C.A. Cooper, R.J. Young, and M.P. Halsall, *Phys. Rev. B* **67**, 035417 (2003).
 - ⁴⁰ C.A. Cooper, R.J. Young, and M. Halsall, *Composites Part A: Applied Science and Manufacturing* **32**, 401 (2001).
 - ⁴¹ M. Lucas and R.J. Young, *Phys. Rev. B* **69**, 085405 (2004).
 - ⁴² U.D. Venkateswaran, A.M. Rao, E. Richter, M. Menon, A. Rinzier, R.E. Smalley, and P.C. Eklund, *Phys. Rev. B* **59**, 10928 (1999).
 - ⁴³ C. Thomsen, S. Reich, H. Jantoljak, I. Loa, K. Syassen, M. Burghard, G.S. Duesberg, and S. Roth, *Appl. Phys. A* **69**, 309 (1999).
 - ⁴⁴ I. Loa, J. Raman Spectrosc. **34**, 611 (2003).
 - ⁴⁵ M. Menon, E. Richter, and K.R. Subbaswamy, *J. Chem. Phys.* **104**, 5875(1996).
 - ⁴⁶ K. Parlinski, Z.-Q. Li, and Y. Kawazoe, *Phys. Rev. Lett.* **78**, 4063 (1997).
 - ⁴⁷ G. Vilianni, R. DellAnna, O. Pilla, M. Montagna, G. Ruocco, G. Signorelli, and V. Mazzacurati, *Phys. Rev. B* **52**, 3346 (1995).
 - ⁴⁸ G. Kresse and J. Hafner, *Phys. Rev. B* **48**, 13115 (1993).
 - ⁴⁹ G. Kresse and J. Furthmüller, *Comput. Mater. Sci.* **6**, 15 (1996); *Phys. Rev. B* **54**, 11 169 (1996).
 - ⁵⁰ P.E. Blöchl, *Phys. Rev. B* **50**, 17 953 (1994).
 - ⁵¹ G. Kresse and D. Joubert, *Phys. Rev. B* **59**, 1758 (1999).
 - ⁵² Ofir E. Alon, *Phys. Rev. B* **63**, 201403(R) (2001).
 - ⁵³ G. Y. Guo, K. C. Chu, Ding-sheng Wang and Chun-gang Duan, *Phys. Rev. B* **69**, 205416 (2004).
 - ⁵⁴ M. Hanfland, H. Beister, and K. Syassen, *Phys. Rev. B* **39**, 12598 (1989).
 - ⁵⁵ A. Kasuya, Y. Sasaki, Y. Saito, K. Tohji, and Y. Nishina, *Phys. Rev. Lett.* **78**, 4434 (1997).
 - ⁵⁶ H. Jiang, G. Wu, X. Yang, and J. Dong, *Phys. Rev. B* **70**, 125404 (2004).
 - ⁵⁷ U.D. Venkateswaran, E.A. Brandesen, U. Schlecht, A.M. Rao, E. Richter, I. Loa, K. Syassen and P.C. Eklund, *Phys. Status Solid B* **223**, 225 (2001).
 - ⁵⁸ B. I. Yakobson, C.J. Brabec, and J. Bernholc, *Phys. Rev.*

Lett. **76**, 2511 (1996).

⁵⁹ M.B. Nardelli, B.I. Yakobson, and J. Bernholc, Phys. Rev.

Lett. **81**, 4656 (1998).